Applied Physics Letters

Resistive switching properties of monolayer h-BN atomristors with different electrodes

Cite as: Appl. Phys. Lett. **120**, 173104 (2022); https://doi.org/10.1063/5.0087717
Submitted: 08 February 2022 • Accepted: 12 April 2022 • Published Online: 27 April 2022

Yuan Li, Zhenjun Cui, Yanwei He, et al.

View Online

Export Citation

CrossMark

Lock-in Amplifiers
up to 600 MHz

Zurich
Instruments

Watch

© 2022 Author(s).

Applied Physics Letters ARTICLE scitation.org/journal/apl

Resistive switching properties of monolayer h-BN atomristors with different electrodes

Cite as: Appl. Phys. Lett. **120**, 173104 (2022); doi: 10.1063/5.0087717
Submitted: 8 February 2022 · Accepted: 12 April 2022 ·
Published Online: 27 April 2022

View Online

Export Citation

CrossMark

Yuan Li, Zhenjun Cui, Yanwei He, Hao Tian, Tianchen Yang, Chengyun Shou, and Jianlin Liu[a)]

AFFILIATIONS

Department of Electrical and Computer Engineering, University of California, Riverside, California 92521, USA

[a)]Author to whom correspondence should be addressed: jianlin@ece.ucr.edu. Tel.: 1-9518277131. Fax: 1-9518272425

ABSTRACT

Resistive switching properties based on molecular beam epitaxy-grown monolayer hexagonal boron nitride (h-BN) atomristors are studied by using metal insulator metal configurations with different electrode materials. Au/monolayer h-BN/Ni devices demonstrate a forming-free bipolar resistive switching (BRS) behavior, a good endurance with up to 97 cycles at a high compliance current of 100 mA, an average on/off ratio of 10^3, and a low set/reset voltage variability. Metal/monolayer h-BN/graphite/Co devices exhibit self-compliant current BRS characteristics. Both metal/h-BN/Ni and metal/h-BN/graphite/Co devices show the coexistence of BRS, unipolar resistive switching (URS), and nonvolatile threshold switching (TH) modes. The formation of conductive filaments is attributed to the diffusion and trapping of metal ions on the defect sites driven by the electric field, while the rupture is driven by the electric field in BRS and by Joule heating in URS and TH modes.

Published under an exclusive license by AIP Publishing. https://doi.org/10.1063/5.0087717

Two-dimensional (2D) materials have drawn tremendous attention for next-generation electronics,[1,2] especially for resistive random access memory (RRAM) in digital information storage and computing due to its simple metal–insulator–metal (MIM) sandwiched structure, excellent switching performance, high-density capability, low-power consumption, and high scalability and compatibility with traditional CMOS technology.[3,4] Resistive switching (RS) capability was demonstrated in transition metal oxide 2D materials in recent years. The basic working principle of resistive memories is based on the reversible conversion between high resistance state (HRS) and low resistance state (LRS) that correspond to zeros and ones in the binary system, through the formation and annihilation of conductive filaments (CFs) in the dielectrics.[5,6]

While resistive memory devices have been widely researched using transition metal oxides as dielectric materials such as HfO_2,[7,8] Al_2O_3,[9] and TiO_2,[10,11] to scale down the active material thickness to atomic level, one promising method is to replace the metal oxide films in the MIM cells by 2D materials with advanced properties. Among all 2D materials, hexagonal boron nitride (h-BN) is one of the ideal RS materials owing to its wide bandgap (∼5.9 eV), high electric breakdown strength (∼12 MV/cm), high thermal conductivity (∼600 W m^{-1} K^{-1}), excellent thermal/chemical stability, and free-dangling bond surface.[12–14] 2D h-BN resistive memories have been intensively studied. Lanza and coworkers exploited multilayer h-BN as an active switching layer with different metal electrodes, demonstrating the formation and rupture of CFs as the origin of the RS behaviors.[15–18] Theoretical calculations on the migration of vacancies and charge carriers in h-BN were also investigated by Zobelli *et al.*, Ranjan *et al.*, and Wu *et al.*, illustrating mechanisms during the set and reset processes.[19–21] Flexible resistive switching devices based on 2D h-BN were developed by Qian *et al.*[22] and Siddiqui *et al.*[23] Despite these developments, there are very limited efforts on atomically thin memristors based on h-BN films with monolayer thickness, namely, monolayer h-BN atomristors.[21,24] Moreover, although a mechanism of the formation and rupture of CFs related to the electric field- and joule heat-driven ion migration has been proposed,[5,21] a more comprehensive understanding concerning different RS behaviors in monolayer h-BN with different electrodes is still required.

In this work, we fabricated two types of monolayer h-BN atomristors by transfer-free vertically stacking metal electrodes onto molecular beam epitaxy (MBE)-grown monolayer h-BN films and monolayer h-BN/graphite heterostructures on metal substrates, namely, metal/monolayer h-BN/Ni and metal/monolayer h-BN/graphite/Co MIM devices, and investigated their resistive switching performance and properties. Direct tunneling conduction, space charge limited current conduction (SCLC), and Ohmic conduction processes were demonstrated in the monolayer h-BN films. Trapping of metal ions in the monolayer h-BN driven by electric field resulted in the formation of CFs, while the rupture of these CFs was dominated

Published under an exclusive license by AIP Publishing

by electric field in bipolar resistive switching (BRS) or controlled by Joule heating in unipolar resistive switching (URS) and threshold (TH) switching. Moreover, self-compliance current BRS phenomena were discovered in h-BN/graphite-based devices, attributing to the large out-of-plane resistance of graphite.

A PerkinElmer MBE system with a background pressure of $\sim 10^{-9}$ Torr was employed to grow monolayer h-BN films and vertical h-BN/graphite heterostructures on mechanically polished Ni and Co substrates, respectively.[14,25,26] Boron oxide (B_2O_3) powder (Alfa Aesar, 99.999% purity) was used as the boron source in an effusion cell, which was kept at 1170 °C during the growth. Nitrogen plasma (Airgas, 99.9999% purity) generated by an electron cyclotron resonance (ECR) system and ammonia gas (American Gas Group, 99.9995% purity) were used as the nitrogen sources. Acetylene gas (Airgas, 99.999% purity) was introduced to enrich substrates with carbon prior to h-BN growth.[25] During the growth, the substrate temperature was maintained at 900 °C–930 °C. A mixture of nitrogen source consisting of N_2 gas flowed at 10 sccm through an ECR plasma generator and NH_3 gas controlled at a flow rate of 5 sccm through a needle valve was introduced into the chamber.[25,27] The detailed growth conditions are summarized in the supplementary material (Table S1 and Fig. S1). Scanning electron microscopy (SEM) images were acquired by an FEI NNS450 system. AFM images were acquired by tapping mode of a Veeco D5000 AFM system. Raman spectra were obtained by a confocal HORIBA LabRam microscope equipped with a 60-mW 532-nm laser. UV-vis absorption spectra were obtained by an Agilent Cary 5000 double beam UV-vis spectrophotometer. XPS spectra were obtained by a Kratos XPS analytical instrument. *I–V* measurements were carried out by an Agilent 4155C semiconductor parameter analyzer.

Figure 1(a) shows an SEM image of the continuous monolayer h-BN film taken at the center of the as-grown sample. The inset is an SEM image of the film at its edge area, showing plenty of triangular h-BN flakes that have not merged to become continuous film. The h-BN triangular flakes and Ni substrate appear in relative dark and light areas, respectively. There are some but sparse bright features across the 1 × 1 cm^2 sample surface due to the formation of adlayers (local multilayer h-BN) in these locations. The thickness of the monolayer h-BN film is confirmed by AFM results as shown in Fig. 1(b). AFM image and the scanning profile were taken across an edge of the transferred h-BN film onto 300-nm SiO_2/Si substrate, indicating a thickness of $\sim$0.6 nm. This value is larger compared with theoretical value ($\sim$0.33 nm) of a single-layer h-BN film due to the AFM cantilever tip effects including different van der Waals bonding of the AFM tip with the h-BN film and SiO_2 surfaces.[28] Figure 1(c) shows a Raman spectrum of the transferred monolayer h-BN film on SiO_2/Si substrate. The characteristic E_{2g} mode peak is found at around 1369 cm^{-1} with a full width at half maximum (FWHM) of $\sim$14 cm^{-1}, implying that the film is a monolayer h-BN.[29] Figure 1(d) shows a UV-vis absorption spectrum of the h-BN film transferred on sapphire substrate and corresponding Tauc plot (assuming a direct bandgap of the monolayer h-BN). A strong peak with a sharp absorption edge is observed at 208 nm, corresponding to a wide optical bandgap of 5.95 eV extracted from the Tauc plot.[30] Figures 1(e) and 1(f) show XPS spectra of B 1s and N 1s signals of as-grown monolayer h-BN. The main peaks of B 1s and N 1s are located around 190.1 and 397.6 eV, respectively, an indication of sp^2 bonds. The much weaker shoulder peaks next to the main peaks at higher energy, 190.7 and 398.2 eV, are assigned to cubic-like sp^3 bonds and oxygen impurity related peaks.[27,31] This is consistent with the SEM result in Fig. 1(a), showing the existence of sparse h-BN adlayer features within the large-area 2D film. The stoichiometry of boron to nitrogen is $\sim$1 within the experimental error of the XPS sensitivity and peak fitting. Similar material characterizations

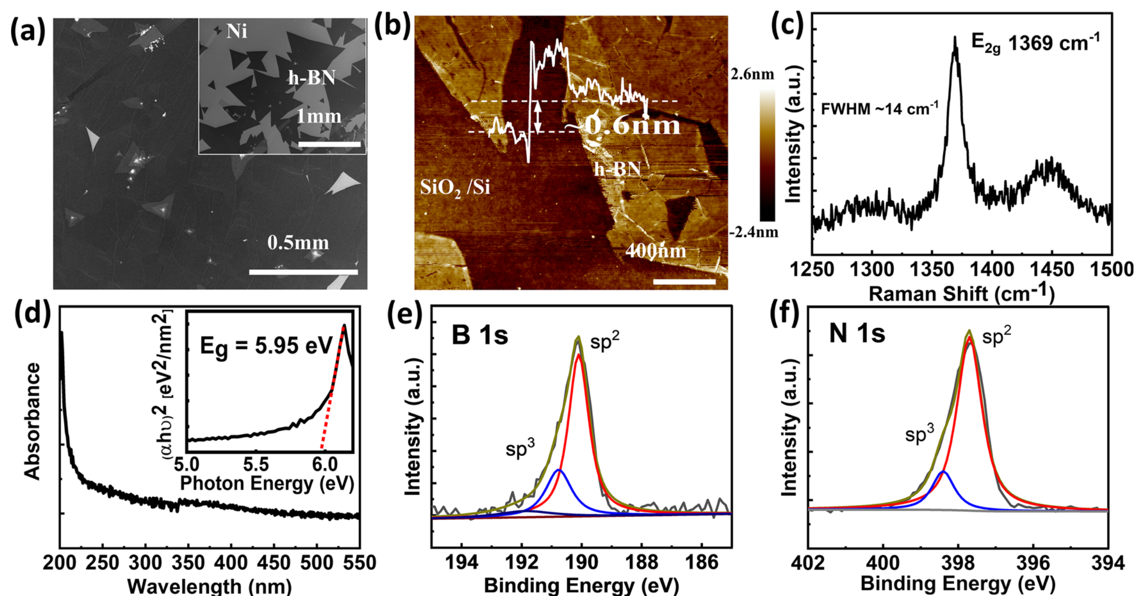

FIG. 1. Characterization of the monolayer h-BN film. (a) SEM image of the continuous h-BN film on Ni substrate. Inset is an image of the sample at the edge area, (b) AFM image and scanning profile across the sample edge on the transferred h-BN film on SiO_2/Si, (c) Raman spectrum measured on the transferred h-BN on SiO_2/Si, (d) UV-vis spectrum of transferred h-BN on sapphire substrate. Inset shows the Tauc plot determining the optical bandgap, (e) and (f) XPS spectra of B 1s and N 1s, respectively.

Published under an exclusive license by AIP Publishing

of monolayer h-BN/graphite heterostructure on Co were carried out by SEM, AFM, Raman, UV-vis absorption, and XPS, and the results are shown in the supplementary material [Figs. S2(a)–S2(f)]. These characterizations demonstrate a heterostructure with monolayer h-BN on the graphite film of ∼132 nm.

The device fabrication procedure using standard photolithography and e-beam evaporation process is schematically shown in Fig. S3 in the supplementary material. Figure 2(a) shows a schematic of the Au/monolayer h-BN/Ni device structure with a size of 50 × 50 μm^2. As shown in Fig. 2(b), by applying electric bias with a compliance current of 100 mA, the device exhibits successive forming-free nonvolatile BRS behavior. A compliance current of 100 mA is a record-high value compared to resistive memories based on monolayer films in literature, suggesting the robustness of the present epitaxial monolayer h-BN film for resistive memory applications. The pristine device is initially at HRS until a positive bias of ∼1 V from active Ni electrode with respect to inert Au electrode is applied to switch the device to LRS, which is referred to as the "SET" process, while the negative bias switches the h-BN from LRS back to HRS, known as "RESET." Also, this behavior is not accompanied by the forming process, and device-to-device set voltage variability is small. Considering the structure of monolayer h-BN, boron vacancies are more energetically favorable and may serve as the localized trapping centers.[19,21,32] While switching from HRS to LRS, due to the migration of Ni metal ions, boron vacancies are filled by these ions, resulting in the formation of CFs and Ohmic-like conduction. Under negative bias, the CFs are ruptured by electric field-driven ion diffusion and/or Joule heating induced filaments melting, resetting the device back to HRS.[5,15,22,23] In addition to the device size 50 × 50 μm^2, Fig. S4 in the supplementary material shows the BRS behaviors of devices with different sizes, namely, 100 × 100, 150 × 150, 200 × 200, and 250 × 250 μm^2, and the resistive switching behaviors do not show any clear trend of the device size dependence. This is reasonable because the conductive filaments are formed locally instead of uniformly distributed across the entire device areas. In an earlier report by Cui *et al.*,[33] the effective tunneling area and breakdown location of h-BN MIM tunneling structures are orders of magnitude smaller than physical area of the devices.

To further study the mechanism of the resistive switching behaviors, the *I–V* characteristics of HRS and LRS are plotted on a double logarithmic scale in Fig. 2(c). In the small bias region (I) of HRS, the *I–V* curves exhibit a typical linear relationship with a slope of ∼1, namely, $I \propto V$, suggesting that the device is operated in a direct tunneling region, which can be described by Simmon's model.[33–36] As the voltage increases further, the *I–V* curves show the quadratic dependence $I \propto V^{\alpha}$, $\alpha = 1.82 \approx 2$ in the moderate voltage region II, followed by the steep current increase (filament formation) region (III) ($I \propto V^{\alpha}$, $\alpha > 2$), which is in good agreement with the characteristics of the trap-controlled SCLC mechanism and is best-fitted by the SCLC model[23,37–40] as $J_{trap-controlled} = \frac{9}{8}\varepsilon_0\varepsilon_r\mu\theta\frac{V^2}{d^3}$, where $J_{trap-controlled}$ is the trap controlled current density, ε_0 is the permittivity of free space, ε_r is the relative dielectric constant, μ is the mobility of charge carriers, and θ is the ratio of free and shallow trapped charge. When the bias exceeds the square-law onset voltage, the density of carriers injected into the traps gradually exceeds the equilibrium concentration and dominates the conduction, where the $I \propto V^2$ region is known as the trap-unfilled SCLC region. As the bias rises to region III, the traps in the monolayer h-BN are continuously filled up with injected ions. Once all the traps are filled, the injected carriers can move freely through the h-BN and consequently result in rapid change of resistance to LRS. The *I–V* curves in the LRS region (IV) exhibit a typical

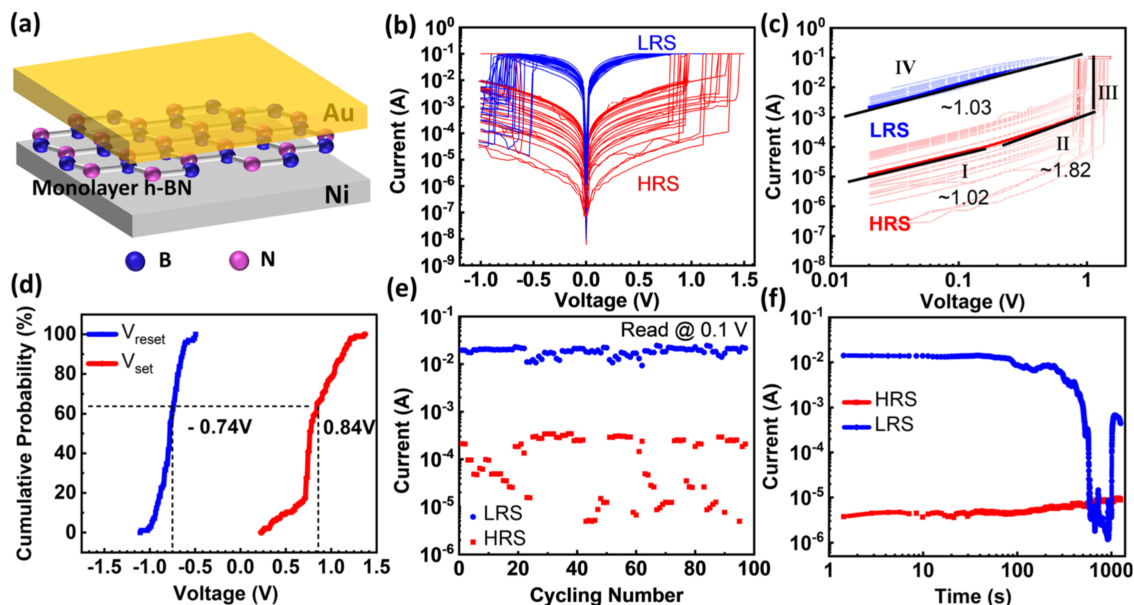

FIG. 2. Resistive switching properties of Au/monolayer h-BN/Ni MIM devices with a size of 50 × 50 μm^2. (a) Schematic of the Au/monolayer h-BN/Ni atomristor structure, (b) *I–V* characteristics of successive bipolar resistive switching, (c) linear fitting of the HRS and LRS *I–V* curves on a double logarithmic scale, (d) cumulative probability of set and reset voltage distributions, (e) the dispersion of both HRS and LRS in terms of the current read at 0.1 V, and (f) the resistive-state retention characteristics of monolayer h-BN atomristor at ambient condition.

Published under an exclusive license by AIP Publishing

linear relationship ($I \propto V$) with a slope of ~1, implying the formation of the metallic conductive filaments during the set process, which is consistent with the Ohmic conduction.

Figure 2(d) shows the cumulative probability of set and reset voltage distribution of Au/monolayer h-BN/Ni devices. By setting the probability to 0.63 according to the Weibull distribution,[41] the estimated characteristic set and reset voltages are 0.84 and −0.74 V, respectively, and the difference of the absolute values ($V_{set} - V_{reset} \approx 0.1V$) is attributed to the built-in voltage at equilibrium between barrier heights of Ni/h-BN and Au/h-BN junctions.[34] The work function of Au is about 0.09 eV larger than that of Ni theoretically,[42] which is in good agreement with the experimental results. The DC cyclability up to 97 sweeping cycles is achieved by maintaining the large on/off current ratio of around 10^3 with good uniformity, as shown in Fig. 2(e). Figure S5 in the supplementary material shows cumulative probability distribution of HRS and LRS resistances of the Au/monolayer h-BN/Ni device read at 0.1 V. At a cumulative probability of 63%, the LRS and HRS resistances are 5.5 Ω and 2.1 × 10^3 Ω, respectively. The long-term resistive-state retention of both HRS and LRS is stable up to 10^3 s with maintaining a resistance ratio approximately 10^3 at ambient condition, indicating good nonvolatile characteristics of the device.

All the monolayer h-BN atomristor devices with different combinations of the metal electrodes (symmetric Ni/Ni and asymmetric Au/Ni and Pt/Ni) exhibit independent coexistence of BRS, URS, and TH behaviors under a compliance current of 100 mA.[43–45] Figures 3(a)–3(i) show representative I–V characteristics of Ni/h-BN/Ni, Au/h-BN/Ni, and Pt/h-BN/Ni devices. In all the BRS behaviors, in the electric bias sweeping from active Ni bottom electrode to inert top metal electrodes, the set and reset processes in symmetric Ni/h-BN/Ni devices show almost identical voltages, while the set voltages are larger than these of reset voltages in asymmetric Au or Pt/h-BN/Ni devices due to the built-in electric field attributed to the different metal work functions among Au, Pt, and Ni. In all the URS and TH behaviors, the set process is also facilitated by the electric field, leading to the formation of localized nanoscale filaments. While in the reset process, the Joule heating generated by current flowing through the devices via numerous nanoscale conductive filaments results in the rupture of CFs, which is elaborated later in Fig. 5.

Figure 4(a) shows a schematic of the metal/monolayer h-BN/graphite/Co devices, and Fig. S6 in the supplementary material shows the optical microscopy image of the fabricated Au/h-BN/graphite/Co devices. Figures 4(b) and 4(c) show bipolar switching characteristics of Co/monolayer h-BN/multilayer graphite/Co and Au/monolayer

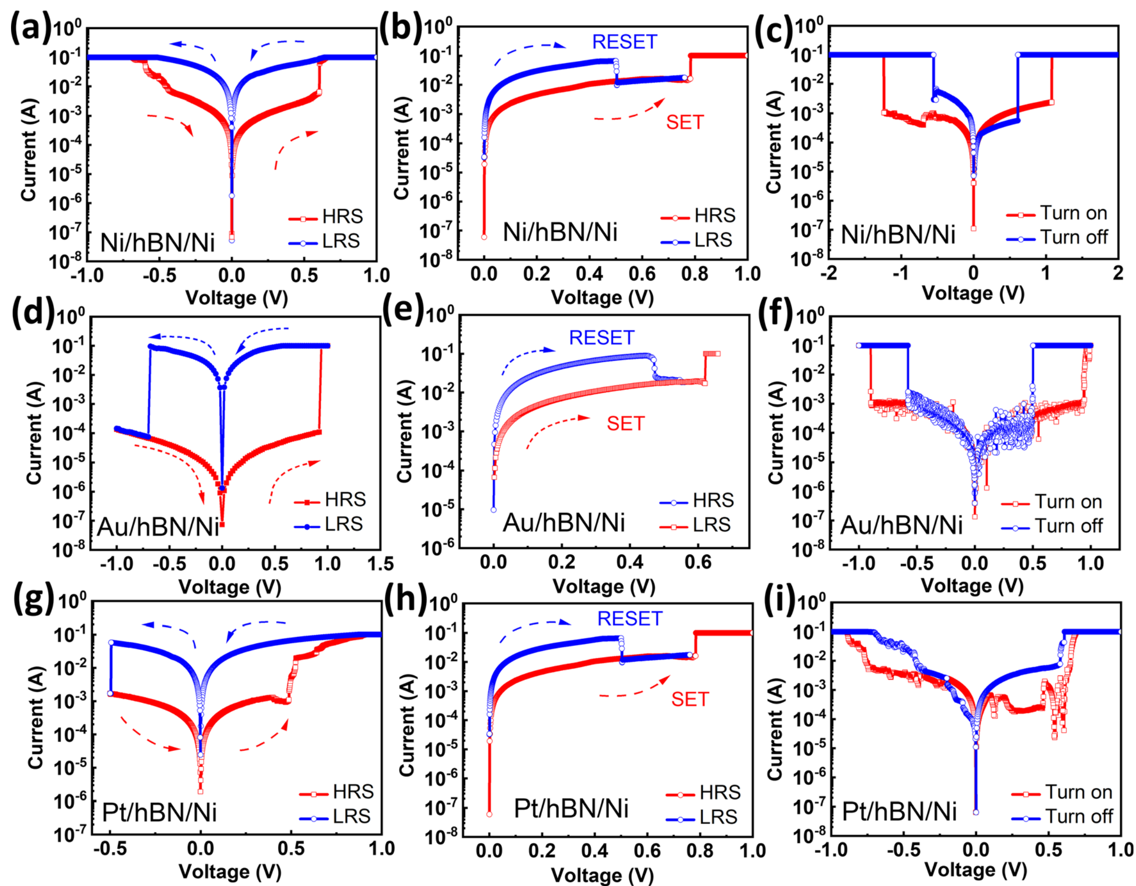

FIG. 3. Coexistence of BRS, URS, and TH switching behaviors in metal/monolayer h-BN/Ni atomristors. (a)–(c) BRS, URS, and TH behaviors in symmetric Ni/h-BN/Ni devices, (d)–(f) BRS, URS, and TH behaviors in asymmetric Au/h-BN/Ni devices, and (g)–(i) BRS, URS, and TH behaviors in asymmetric Pt/h-BN/Ni devices.

Published under an exclusive license by AIP Publishing

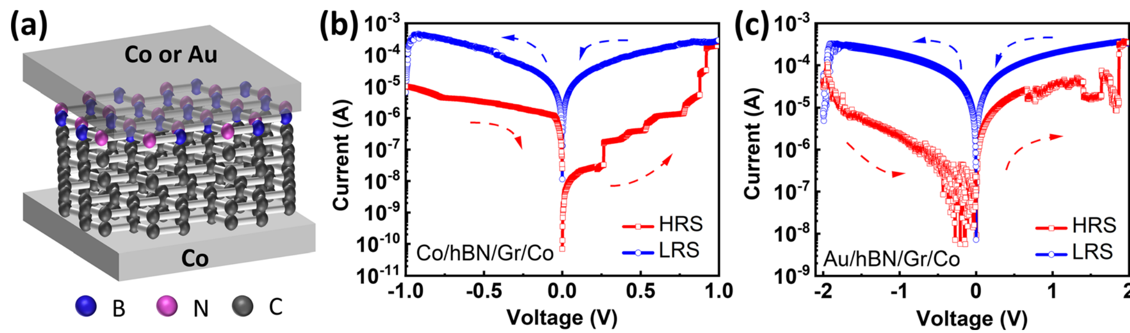

FIG. 4. (a) Schematic of metal (Co or Au)/monolayer h-BN/graphite/Co devices. The blue and purple layers represent the monolayer h-BN, and the gray layers represent the multilayer graphite, (b) self-compliance current bipolar resistive switching in Co/monolayer h-BN/multilayer graphite/Co device, and (c) self-compliance current resistive switching in Au/monolayer h-BN/multilayer graphite/Co device.

h-BN/multilayer graphite/Co devices, respectively. Unlike most cases of resistive switching settings that require external current compliance (100 mA) to prevent the hard breakdown of the dielectrics, self-compliance current BRS phenomenon is discovered in these metal/monolayer h-BN/graphite/Co devices. This phenomenon suggests a significant increase in the resistance in the devices during the operation, which may be caused by the existence of internal resistance of the graphite in series with the resistance of the h-BN film. The basic crystal structure of graphite is the stacking of honeycomb network, i.e., an extended hexagonal array of carbon atoms with sp^2 σ bonding and delocalized π bonding. Also, the spacing between layers (3.4 Å) is about 2.4 times the distance between the adjacent carbon atoms in a layer (1.42 Å), resulting in the large anisotropy of the electrical conductivity in graphite, where out-of-plane conductivity is around four orders of magnitude smaller than that of in-plane.[46,47] An estimation of the self-compliance resistance from the I–V experimental data in Figs. 4(b) and 4(c) yields high resistance $\sim 10^4\,\Omega$, which is in good agreement with the theoretical resistance calculation of graphite based on $R = \frac{\rho L}{A}$. This suggests that the high resistance from graphite hinders the transport and migration of carriers, leading to the self-compliance BRS property of the metal/h-BN/graphite/Co devices. In addition to BRS behaviors, URS and TH switching characteristics were also demonstrated in these metal/monolayer h-BN/graphite/Co devices, as shown in Fig. S7 in the supplementary material.

Figure 5 shows schematic of the physical mechanism behind the resistive switching of the monolayer h-BN atomristors between HRS and LRS. As discussed before, monolayer h-BN would intrinsically contain defects, such as boron vacancies [Fig. 5(a)]. During the set process, by applying a bias, metal ions will be trapped at the defect sites in the monolayer h-BN film [Fig. 5(b)], forming a conductive path in the vertical direction to establish the LRS shown in Fig. 5(c). By applying the opposite DC bias in the BRS mode, the device is switched back to pristine HRS in the reset process as shown in Fig. 5(d). De-trapping of the defects is driven by the electric field, which causes the rupture of the CFs. On the other hand, during the reset processes in the unipolar and threshold resistive switching modes under the same voltage polarity as that of the set processes, the rupture of the filaments is dominated by Joule heating, followed by Fick's diffusion of metal ions at high temperatures. Current flowing through the devices via numerous nanoscale conductive filaments will inevitably produce Joule heating along the conduction paths, which significantly raises the temperature locally around the filament region or localized trapping sites. Conductive ions will diffuse away from the filament region driven by the concentration gradient and mediated by the increase in mobility at high temperatures, thus dissolving the conductive filaments.

In summary, resistive switching properties are studied based on the monolayer h-BN atomristors with different metal/h-BN/Ni and metal/h-BN/graphite/Co structures. All devices exhibit independent coexistence of forming-free nonvolatile BRS, URS, and volatile TH switching behaviors. The BRS performance exhibits a good endurance with nearly 100 DC voltage-sweeping cycles at a high compliance current of 100 mA, an average on/off window of 10^3, low set and reset voltage variabilities, and worthy improved retention time at the ambient condition with good uniformity. Devices show work function-related set/reset voltages. Moreover, devices with graphite in between h-BN and metal electrodes demonstrate self-compliant current BRS mode. Ohmic conduction and space charge limited current

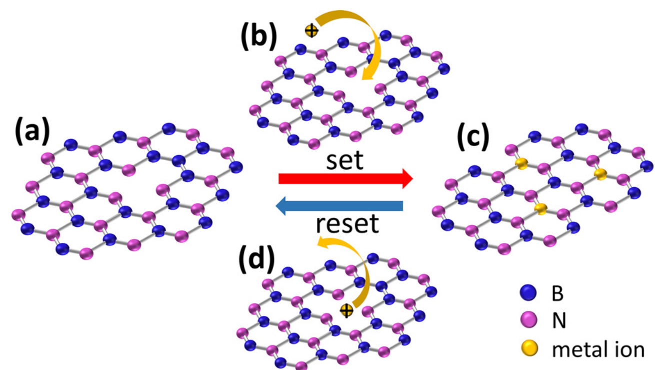

FIG. 5. Schematics of resistive switching mechanisms in monolayer h-BN atomristor. Top electrodes are Ni, Au, and Pt in metal/h-BN/Ni devices and are Co and Au in metal/h-BN/graphite/Co devices. Blue, purple, and yellow spheres represent boron atoms, nitrogen atoms, and metal ions, respectively. (a) Pristine HRS of monolayer h-BN. The hollows in the monolayer h-BN are non-conductive defects or traps such as boron vacancies, (b) the set process of h-BN from HRS to LRS, showing the migration of metal ions driven by the electric field, (c) the LRS of monolayer h-BN, showing the metal ions substituting into the boron vacancies, resulting in the formation of CFs, and (d) the reset process of h-BN from LRS to HRS, showing the de-trapping of metal ions driven by electric field or Joule heating, leading to the rupture of the CFs, and switching back to HRS.

Published under an exclusive license by AIP Publishing

conduction mechanisms are observed in LRS and HRS the in BRS mode, respectively. Trapping metal ions in the defects within the monolayer h-BN layer result in the formation of CFs driven by the electric field, while the rupture of CFs is dominated by the electric field in BRS or controlled by Joule heating in URS and TH switching. Our work provides an understanding of the resistive switching properties in the atomically thin h-BN resistive memories with different electrodes and, thus, sheds light on the potential application of these thinnest layers for future RRAM technologies.

See the supplementary material for the detailed results of MBE growth of monolayer h-BN and h-BN/graphite heterostructure, materials characterization of the h-BN/graphite film, h-BN atomristor devices fabrication, BRS characteristics of Au/h-BN/Ni devices with different sizes, cumulative probability of HRS and LRS resistances of an Au/h-BN/Ni device, optical microscopy image of fabricated Au/h-BN/graphite/Co devices, and the *I*–*V* results of coexistence of BRS, URS, and TH behaviors in metal/h-BN/graphite/Co devices.

This work was supported by Spins and Heat in Nanoscale Electronic Systems, an Energy Frontier Research Center funded by the U.S. Department of Energy, The Office of Science, Basic Energy Sciences Division, under Award No. SC0012670, and by the University of California, Riverside Academic Senate Committee on Research grant.

AUTHOR DECLARATIONS

Conflict of Interest

The authors have no conflicts to disclose.

DATA AVAILABILITY

The data that support the findings of this study are available from the corresponding author upon reasonable request.

REFERENCES

[1] G. Fiori, F. Bonaccorso, G. Iannaccone, T. Palacios, D. Neumaier, A. Seabaugh, S. K. Banerjee, and L. Colombo, Nat. Nanotechnol. **9**, 768 (2014).
[2] D. Akinwande, C. Huyghebaert, C.-H. Wang, M. I. Serna, S. Goossens, L.-J. Li, H.-S. P. Wong, and F. H. L. Koppens, Nature **573**, 507 (2019).
[3] J. S. Lee, S. Lee, and T. W. Noh, Appl. Phys. Rev. **2**, 031303 (2015).
[4] H.-S. P. Wong, H.-Y. Lee, S. Yu, Y.-S. Chen, Y. Wu, P.-S. Chen, B. Lee, F. T. Chen, and M.-J. Tsai, Proc. IEEE **100**, 1951 (2012).
[5] Y. Yang and W. Lu, Nanoscale **5**, 10076 (2013).
[6] Y. Li, S. Long, Q. Liu, H. Lv, and M. Liu, Small **13**, 1604306 (2017).
[7] U. Chand, K.-C. Huang, C.-Y. Huang, C.-H. Ho, C.-H. Lin, and T.-Y. Tseng, J. Appl. Phys. **117**, 184105 (2015).
[8] C. Li, B. Gao, Y. Yao, X. Guan, X. Shen, Y. Wang, P. Huang, L. Liu, X. Liu, J. Li, C. Gu, J. Kang, and R. Yu, Adv. Mater. **29**, 1602976 (2017).
[9] M. Y. Yang, K. Kamiya, B. Magyari-Köpe, M. Niwa, Y. Nishi, and K. Shiraishi, Appl. Phys. Lett. **103**, 093504 (2013).
[10] H. Y. Jeong, J. Y. Lee, and S.-Y. Choi, Adv. Funct. Mater. **20**, 3912 (2010).
[11] K. Kamiya, M. Y. Yang, T. Nagata, S.-G. Park, B. Magyari-Köpe, T. Chikyow, K. Yamada, M. Niwa, Y. Nishi, and K. Shiraishi, Phys. Rev. B **87**, 155201 (2013).
[12] L. Song, L. Ci, H. Lu, P. B. Sorokin, C. Jin, J. Ni, A. G. Kvashnin, D. G. Kvashnin, J. Lou, B. I. Yakobson, and P. M. Ajayan, Nano Lett. **10**, 3209 (2010).
[13] L. Wang, X. Xu, L. Zhang, R. Qiao, M. Wu, Z. Wang, S. Zhang, J. Liang, Z. Zhang, Z. Zhang, W. Chen, X. Xie, J. Zong, Y. Shan, Y. Guo, M. Willinger, H. Wu, Q. Li, W. Wang, P. Gao, S. Wu, Y. Zhang, Y. Jiang, D. Yu, E. Wang, X. Bai, Z.-J. Wang, F. Ding, and K. Liu, Nature **570**, 91 (2019).
[14] Y. He, H. Tian, P. Das, Z. Cui, P. Pena, I. Chiang, W. Shi, L. Xu, Y. Li, T. Yang, M. Isarraraz, C. S. Ozkan, M. Ozkan, R. K. Lake, and J. Liu, ACS Appl. Mater. Interfaces **12**, 35318 (2020).
[15] C. Pan, Y. Ji, N. Xiao, F. Hui, K. Tang, Y. Guo, X. Xie, F. M. Puglisi, L. Larcher, E. Miranda, L. Jiang, Y. Shi, I. Valov, P. C. McIntyre, R. Waser, and M. Lanza, Adv. Funct. Mater. **27**, 1604811 (2017).
[16] F. Hui, M. A. Villena, W. Fang, A.-Y. Lu, J. Kong, Y. Shi, X. Jing, K. Zhu, and M. Lanza, 2D Mater. **5**, 031011 (2018).
[17] X. Jing, F. Puglisi, D. Akinwande, and M. Lanza, 2D Mater. **6**, 035021 (2019).
[18] M. Lanza, H.-S. P. Wong, E. Pop, D. Ielmini, D. Strukov, B. C. Regan, L. Larcher, M. A. Villena, J. J. Yang, L. Goux, A. Belmonte, Y. Yang, F. M. Puglisi, J. Kang, B. Magyari-Köpe, E. Yalon, A. Kenyon, M. Buckwell, A. Mehonic, A. Shluger, H. Li, T.-H. Hou, B. Hudec, D. Akinwande, R. Ge, S. Ambrogio, J. B. Roldan, E. Miranda, J. Suñe, K. L. Pey, X. Wu, N. Raghavan, E. Wu, W. D. Lu, G. Navarro, W. Zhang, H. Wu, R. Li, A. Holleitner, U. Wurstbauer, M. C. Lemme, M. Liu, S. Long, Q. Liu, H. Lv, A. Padovani, P. Pavan, I. Valov, X. Jing, T. Han, K. Zhu, S. Chen, F. Hui, and Y. Shi, Adv. Electron. Mater. **5**, 1800143 (2019).
[19] A. Zobelli, C. P. Ewels, A. Gloter, and G. Seifert, Phys. Rev. B **75**, 094104 (2007).
[20] A. Ranjan, N. Raghavan, S. J. O'Shea, S. Mei, M. Bosman, K. Shubhakar, and K. L. Pey, Sci. Rep. **8**, 2854 (2018).
[21] X. Wu, R. Ge, P.-A. Chen, H. Chou, Z. Zhang, Y. Zhang, S. Banerjee, M.-H. Chiang, J. C. Lee, and D. Akinwande, Adv. Mater. **31**, 1806790 (2019).
[22] K. Qian, R. Y. Tay, V. C. Nguyen, J. Wang, G. Cai, T. Chen, E. H. T. Teo, and P. S. Lee, Adv. Funct. Mater. **26**, 2176 (2016).
[23] G. U. Siddiqui, M. M. Rehman, Y.-J. Yang, and K. H. Choi, J. Mater. Chem. C **5**, 862 (2017).
[24] R. Ge, X. Wu, M. Kim, J. Shi, S. Sonde, L. Tao, Y. Zhang, J. C. Lee, and D. Akinwande, Nano Lett. **18**, 434 (2018).
[25] A. Khanaki, H. Tian, Z. Xu, R. Zheng, Y. He, Z. Cui, J. Yang, and J. Liu, Nanotechnology **29**, 035602 (2018).
[26] H. Tian, A. Khanaki, P. Das, R. Zheng, Z. Cui, Y. He, W. Shi, Z. Xu, R. Lake, and J. Liu, Nano Lett. **18**, 3352 (2018).
[27] Y. He, H. Tian, A. Khanaki, W. Shi, J. Tran, Z. Cui, P. Wei, and J. Liu, Appl. Surf. Sci. **498**, 143851 (2019).
[28] M. H. Khan, Z. Huang, F. Xiao, G. Casillas, Z. Chen, P. J. Molino, and H. K. Liu, Sci. Rep. **5**, 7743 (2015).
[29] R. V. Gorbachev, I. Riaz, R. R. Nair, R. Jalil, L. Britnell, B. D. Belle, E. W. Hill, K. S. Novoselov, K. Watanabe, T. Taniguchi, A. K. Geim, and P. Blake, Small **7**, 465 (2011).
[30] C. Elias, P. Valvin, T. Pelini, A. Summerfield, C. J. Mellor, T. S. Cheng, L. Eaves, C. T. Foxon, P. H. Beton, S. V. Novikov, B. Gil, and G. Cassabois, Nat. Commun. **10**, 2639 (2019).
[31] M. Schwarz, A. Riss, M. Garnica, J. Ducke, P. S. Deimel, D. A. Duncan, P. K. Thakur, T.-L. Lee, A. P. Seitsonen, J. V. Barth, F. Allegretti, and W. Auwärter, ACS Nano **11**, 9151 (2017).
[32] S. Okada, Phys. Rev. B **80**, 161404 (2009).
[33] Z. Cui, Y. He, H. Tian, A. Khanaki, L. Xu, W. Shi, and J. Liu, ACS Appl. Electron. Mater. **2**, 747 (2020).
[34] Y. He, Y. Li, M. Isarraraz, P. Pena, J. Tran, L. Xu, H. Tian, T. Yang, P. Wei, C. S. Ozkan, M. Ozkan, and J. Liu, ACS Appl. Nano Mater. **4**, 5685 (2021).
[35] J. G. Simmons, J. Appl. Phys. **34**, 1793 (1963).
[36] J. G. Simmons, J. Appl. Phys. **35**, 2655 (1964).
[37] A. Rose, Phys. Rev. **97**, 1538 (1955).
[38] R. H. Bube, J. Appl. Phys. **33**, 1733 (1962).
[39] P. N. Murgatroyd, J. Phys. D: Appl. Phys. **3**, 151 (1970).
[40] A. A. Grinberg, S. Luryi, M. R. Pinto, and N. L. Schryer, IEEE Trans. Electron Devices **36**, 1162 (1989).
[41] C. Chauvet and C. Laurent, IEEE Trans. Electr. Insul. **28**, 18 (1993).
[42] G. N. Derry, M. E. Kern, and E. H. Worth, J. Vac. Sci. Technol., A **33**, 060801 (2015).
[43] L. Goux, J. G. Lisoni, M. Jurczak, D. J. Wouters, L. Courtade, and C. Muller, J. Appl. Phys. **107**, 024512 (2010).
[44] X.-C. Yuan, J.-L. Tang, H.-Z. Zeng, and X.-H. Wei, Nanoscale Res. Lett. **9**, 268 (2014).
[45] D. Choi and C. S. Kim, Appl. Phys. Lett. **104**, 193507 (2014).
[46] K. S. Krishnan and N. Ganguli, Nature **144**, 667 (1939).
[47] A. K. Dutta, Phys. Rev. **90**, 187 (1953).

Published under an exclusive license by AIP Publishing